Dust Impacts on the 2012 Hurricane Nadine Track during the NASA HS3 Field Campaign

E. P. Nowottnick[1,2], P. R. Colarco[2], S. A. Braun[3], D. O. Barahona[4], A. da Silva[4], D. L. Hlavka[5,3], M. J. McGill[3], J. R. Spackman[6]

Corresponding Author: Edward P. Nowottnick – edward.p.nowottnick@nasa.gov

1 GESTAR/Universities Space Research Association, Columbia, MD, 21046, USA

2 Atmospheric Chemistry and Dynamics Laboratory, Code 614, NASA GSFC, Greenbelt, MD, 20771, USA

3 Mesoscale Atmospheric Processes Laboratory, Code 612, NASA GSFC, Greenbelt, MD, 20771, USA

4 Global Modeling and Assimilation Office, Code 610.1, NASA GSFC, Greenbelt, MD, 20771, USA

5 Science Systems and Applications, Inc., Lanham, MD, 20706, USA

6 NASA ARC, Moffett Field, CA, 94035, USA

Abstract:

During the 2012 deployment of the NASA Hurricane and Severe Storm Sentinel (HS3) field campaign, several flights were dedicated to investigating Hurricane Nadine. Hurricane Nadine developed in close proximity to the dust-laden Saharan Air Layer, and is the fourth longest-lived Atlantic hurricane on record, experiencing two strengthening and weakening periods during its 22-day total lifecycle as a tropical cyclone. In this study, the NASA GEOS-5 atmospheric general circulation model and data assimilation system was used to simulate the impacts of dust during the first intensification and weakening phases of Hurricane Nadine using a series of GEOS-5 forecasts initialized during Nadine's intensification phase (12 September 2012). The forecasts explore a hierarchy of aerosol interactions within the model: no aerosol interaction, aerosol-radiation interactions, and aerosol-radiation and aerosol-cloud interactions simultaneously, as well as variations in assumed dust optical properties. When only aerosol-radiation interactions are included, Nadine's track exhibits sensitivity to dust shortwave absorption, as a more absorbing dust introduces a shortwave temperature perturbation that impacts Nadine's structure and steering flow, leading to a northward track divergence after 5 days of simulation time. When aerosol-cloud interactions are added, the track exhibits little sensitivity to dust optical properties. This result is attributed to enhanced longwave atmospheric cooling from clouds that counters shortwave atmospheric warming by dust surrounding Nadine, suggesting that aerosol-cloud interactions are a more significant influence on Nadine's track than aerosol-radiation interactions. These findings demonstrate that tropical systems, specifically their track, can be impacted by dust interaction with the atmosphere.

1. Introduction

During northern hemisphere summer, African Easterly Waves (AEWs) originating from continental North Africa can develop into tropical disturbances that propagate westward to the tropical North Atlantic (Burpee et al. 1974; Thorncroft et al. 2001; Kiladas et al. 2006; Chen et al. 2008). Often, these disturbances develop in close proximity to the dry Saharan Air Layer (SAL), which is frequently laden with dust aerosols (Carlson and Prospero, 1972; Karyampudi, 1999) and are advected westward as part of propagating AEWs (Jones et al. 2003; Wong et al. 2009; Knippertz et al. 2010). Recently, there has been increased interest in understanding how dust aerosols within the SAL interact with developing tropical disturbances originating from Africa (Dunion and Velden 2004; Reale et al. 2009; Reale et al. 2011). However, despite several efforts to determine how dust interacts with these disturbances, our understanding remains uncertain, as there are conflicting findings as to whether dust acts to inhibit or enhance tropical cyclogenesis, and to the specific mechanisms that drive dust-tropical cyclogenesis interaction.

The dust laden SAL can impact tropical cyclogenesis interacting directly with radiation and indirectly with cloud processes. Aerosol-radiation impacts include perturbations to storm dynamics caused by the scattering and absorption of light by dust within or near a tropical system. Dunion and Velden (2004) suggested that the warm and dry SAL serves as a mechanism for increased atmospheric stability, which can be augmented by heating within the SAL dust layer by dust absorption of solar and infrared radiation, with dust thus acting to inhibit tropical cyclogenesis. Similarly, Reale (2009, 2011) found that dusty SAL intrusions into a developing tropical system increase atmospheric stability by inducing a heating dipole with warming aloft and cooling below due to absorption within the elevated dust layer. Evan et al. (2006, 2008) and

Lau and Kim (2007) found that Saharan dust outbreaks and tropical cyclogenesis were anti-correlated and both Evan et al. (2008) and Lau and Kim (2007) suggested that solar absorption by dust reduces sea surface temperatures (SSTs), serving as a mechanism for inhibiting tropical cyclogenesis. In contrast, Bretl et al. (2015) found that permitting dust aerosol-radiation interaction had no influence on the number of developing versus non-developing tropical disturbances using an aerosol-climate model. Similarly, Braun et al. (2013) found observational evidence that the dusty SAL had little apparent impact on the development of Hurricane Helene (2006), despite a significant presence during storm development.

Aerosol-cloud interactions between dust and tropical cyclogenesis include modification of cloud and precipitation processes due to the presence of dust. Rosenfeld et al. (2001), DeMott et al. (2003), and Twohy (2015) found observational evidence that dust readily serves as cloud condensation nuclei (CCN) or ice nucleating particles (INP), thereby providing a mechanism for dust to impact cloud microphysics and precipitation. Rosenfeld et al. (2001) found that dust-produced CCN reduce cloud-particle effective radii and, ultimately, impact precipitation. More recently, however, several studies have been focused on understanding the interaction between dust and cloud processes for tropical systems. In a series of idealized model simulations, Zhang et al. (2007) showed that dust acting as CCN can reduce mean cloud droplet diameter, impacting storm diabatic heating, thermodynamic structure, and intensity. On the other hand, Jenkins et al. (2008) and Jenkins and Pratt (2008) found observational evidence that Saharan dust can invigorate precipitation by serving as CCN and IN, suggesting that dust entrainment serves as a mechanism for enhancing tropical convection.

In this study, we investigate aerosol-radiation and aerosol-cloud interaction between dust and Hurricane Nadine (2012) during its first intensification and weakening phases. Hurricane

Nadine developed from an AEW in close proximity to a dust-laden SAL, and was the fourth longest-lived Atlantic hurricane on record, experiencing two strengthening and weakening periods during its lifetime (Braun et al. 2016). We focus on Hurricane Nadine because it was coincident with the first deployment of the NASA Hurricane and Severe Storm Sentinel (HS3) field campaign, which provided airborne observations of dust vertical profiles in conjunction with in-situ meteorological observations. While Munsell et al. (2015) explored the sensitivity of Nadine's simulated track to an ensemble of dynamically perturbed boundary conditions, the impacts of dust on Hurricane Nadine have yet to be explored.

We investigate the impacts of dust on the first intensification and weakening phases of Hurricane Nadine using simulations performed with the NASA Goddard Earth Observing System version 5 (GEOS-5) atmospheric general circulation model and data assimilation system to explore the impacts of dust during the first intensification and weakening phases of Hurricane Nadine. In a series of high spatial resolution GEOS-5 simulations, we initialize from the meteorological analysis state and simulate Nadine without any aerosol-atmosphere interaction, with only direct (aerosol-radiation) interaction (i.e. absorption and scattering) with the atmosphere, and with both direct and indirect (i.e. aerosol-cloud interaction) interaction using a two-moment cloud microphysics scheme that has recently been implemented within GEOS-5 (Barahona et al. 2014). Additionally, we explore the sensitivity of Nadine to dust absorption by varying the assumed dust optical properties in the simulations that permit aerosol-radiation interaction and both aerosol-radiation and aerosol-cloud interaction in order to explore the sensitivity of Nadine to dust absorption. This work is novel in that it presents global high-resolution simulations of a tropical system with various considerations for how dust is permitted to interact with the atmosphere. Moreover, while several previous studies have been focused on dust interactions during the development phase of tropical cyclogenesis, our results are the first to focus on exploring the role of dust during the intensification and weakening phases of a tropical system.

In Section 2, we present an overview of the NASA HS3 field campaign. Section 3 provides a description of the data products used in our analysis, and Section 4 provides a description of the GEOS-5 modeling system and an overview of our simulation setup. Results and a subsequent discussion of the radiative impacts of dust on Hurricane Nadine are provided in Sections 5 and 6, respectively. Conclusions are provided in Section 7.

2. The NASA HS3 Field Campaign

From 2012-2014, the NASA HS3 Earth Venture Suborbital (EV-S) airborne field campaign (https://espo.nasa.gov/hs3/) was based at the NASA Wallops Flight Facility (WFF) in Wallops Island, Virginia. HS3 was focused on improving the understanding of the processes that impact tropical cyclogenesis and intensity change and utilized two NASA unmanned Global Hawk aircraft flying at a high altitude (~20 km) with long range (~20,000 km), equipped with "environmental" and "over-storm" payloads, respectively (Braun et al. 2016). During the 2012 deployment, the environmental payload flew over Hurricane Nadine 5 times (11-12, 14-15, 19-20, 22-23, and 26-27 September) with the goals of examining the impact of the SAL on intensity change, the interaction of the storm with environmental shear, and outflow-layer characteristics. Owing to the long flight range provided by the Global Hawk and duration of up to 26 hours, the environmental payload was able to observe the evolution of Hurricane Nadine from an AEW off the coast of Africa through its two strengthening and one of its weakening phases. For our analysis, we utilize two instruments from the environmental payload, the Cloud Physics Lidar

(CPL) (McGill et al. 2002) and the Advanced Vertical Atmospheric Profiling System (AVAPS) dropsonde system (Hock and Franklin 1999).

3. Data Sources

3.1 CPL

CPL is a multi-wavelength (355, 532, 1064 nm) high-repetition rate (5 kHz) elastic backscatter lidar developed at NASA Goddard Space Flight Center (GSFC) to measure the vertical profiles of clouds and aerosols from high altitude aircraft (McGill et al. 2002). Primary CPL measurements include the total attenuated backscatter at each wavelength and depolarization ratio at 1064 nm. CPL data is provided at 200 m resolution in the horizontal and 30 m in the vertical (McGill et al. 2002). During the HS3 campaign, CPL provided observations of dust vertical profiles and their proximity to developing tropical systems.

3.2 AVAPS

AVAPS dropsondes provide vertical profiles of temperature, pressure, relative humidity, wind speed, and wind direction with a sampling frequency of 0.5 seconds at altitudes up to 24 km (Hock and Franklin 1999). During HS3, up to 88 dropsondes were used per flight to characterize storm intensity, storm outflow, and environmental characteristics, including identification of the SAL.

3.3 MODIS

The Moderate Resolution Imaging Spectroradiometer (MODIS) instruments onboard the sun-synchronous, polar orbiting NASA Terra (10:30 A.M. local equator crossing time) and Aqua (13:30 P.M. local equator crossing time) satellites provide column retrievals of aerosol optical thickness (AOT) at a nominal 10×10 km^2 horizontal resolution. Here we use gridded MODIS

Terra Level 3 AOT retrievals at 550 nm from collection 5.1 algorithms (Remer et al., 2005; Levy et al., 2010).

4. The NASA GEOS-5 Model and Simulation Setup

The NASA GEOS-5 Earth system model and data assimilation system, developed by the NASA Goddard Global Modeling and Assimilation Office (GMAO), provides simulations of weather and climate for NASA instrument teams and the scientific community (Rienecker at al. 2008). In addition to traditional meteorological quantities, such as winds and temperature, GEOS-5 simulates atmospheric composition, notably aerosols (Colarco et al. 2010), which can be radiatively coupled to the atmosphere (Chou and Suarez 1994; Colarco et al. 2014). A near-real time forward processing (FP) and data assimilation system is run at GMAO, which includes traditional meteorological data assimilation (Reinecker et al. 2008) and assimilation of aerosols based on satellite-derived AOT products (Buchard et al. 2015; Nowottnick et al. 2015; Randles et al. 2017; Buchard et al. 2017). Additionally, Nowottnick et al. (2015) describes the GEOS-5 lidar signal simulation capability. Owing to these forecasting and data assimilation capabilities, GEOS-5 forecasts were a valuable resource for guiding mission operations and flight planning involving dusty SAL outbreaks during HS3, and the same modeling system forms the basis of the subsequent scientific analysis presented here.

Aerosols are simulated in GEOS-5 with an online version of the Goddard Chemistry, Aerosol, Radiation, and Transport (GOCART) model (Chin et al. 2002; Colarco et al. 2010). GOCART simulates emission and removal processes of five aerosol species: dust, sea salt, sulfate, black carbon, and organic carbon. Dust is partitioned into 5 non-interacting size bins that span 0.1 and 10 μm in radius. A more in-depth description of the treatment of dust in GEOS-5 is provided in Nowottnick et al. (2010, 2011) and Colarco et al. (2014). Dust optical properties are derived by assuming a spheroidal particle shape distribution and are drawn from a pre-computed database of non-spherical dust particle properties (Meng et al. 2010), as described in Colarco et al. (2014). For the Nadine simulations, we consider two sets of refractive indices for dust, an observationally derived set of refractive indices described in Colarco et al. (2014), and refractive indices from the Optical Properties of Aerosols and Clouds database (OPAC) (Hess et al. 1998), the latter of which are more absorbing at shortwave wavelengths with a 550 nm single scattering albedo of 0.88 compared to 0.92 for the dust optical properties derived from observations (Colarco et al. 2014). Our consideration of two sets of dust optical properties are meant to explore the sensitivity of Nadine to dust absorption and represent uncertainty associated with measurements of the dust refractive index (Balkanski et al. 2007) owing to different minerology associated with various dust source regions, as well as external and internal dust mixtures. Aerosol optical quantities (e.g. extinction, backscatter) are determined from the simulated aerosol mass using pre-computed look-up tables that provide mass and backscattering efficiencies, particulate depolarization ratio, and phase function, all as a function of wavelength, relative humidity, and dry particle size.

Recently, efforts have been made to parameterize aerosol-cloud interaction via an implementation of a two-moment cloud microphysics scheme for stratiform (Morrison and Gettelman, 2008) and convective clouds (Barahona, et al. 2014) in GEOS-5, which explicitly calculates the microphysical processes that impact cloud droplets and ice crystals. Simulated aerosol mass is converted to number concentrations for activation using log-normal size distribution parameters from Lance (2004). In the two-moment cloud microphysics scheme formulation, both homogenous and heterogeneous freezing is permitted, and the ice number concentrations are functions of the atmospheric state, updraft velocity, deposition coefficient, and aerosol number concentrations (Barahona et al., 2010a).

In the current formulation of the two-moment microphysics scheme in GEOS-5, dust is activated as ice nuclei in the immersion and contact modes (Barahona et al. 2014). This means that the partitioning between liquid and ice within convective and stratiform clouds is linked to the presence of dust and other INP. It should be noted that other aerosol species in the model can serve as cloud condensation nuclei (Barahona et al. 2014), and the number concentrations of sulfate, sea salt and organic CCN exceeds those of dust by several orders of magnitude. Therefore, in this configuration, it is expected that dust would serve a more significant role acting as INP than as CCN during the storm development.

To investigate dust impacts on Hurricane Nadine, we consider five baseline aerosol forecast experiments, all initialized from the same GEOS-5 FP assimilation analysis state of aerosols and meteorology. The subsequent evolution of the aerosol distributions in each forecast experiment is then controlled by emission, transport, and removal processes simulated in GOCART, and not impacted by any further aerosol or meteorological data assimilation. Our forecast experiments were run at a global ~25 km horizontal resolution on a cubed-sphere grid (Putman and Suarez 2011), with 72 vertical levels that are terrain following near the surface and transitioning to pressure-following at about 180 hPa, with a model top of ~85 km. We also use results from the GEOS-5 FP analysis over the period of this event.

The specific aerosol-atmosphere interactions considered are outlined in Table 1. The first simulation was run with no interaction (NI) between aerosols and the atmosphere. Next, interaction between aerosols and radiation is considered, using weakly absorbing observation-based (WA) and strongly absorbing OPAC (SA) dust optical properties. Finally, simulations that use both the radiation and two-moment cloud microphysics scheme are conducted in order to investigate aerosol-cloud-radiation interaction with our weakly (WACM) and strongly (SACM) absorbing dust optical properties. It should be noted that the simulations do not permit interaction between the atmosphere and ocean, and that simulations are forced with sea surface temperatures (SSTs) from the Operational Sea Surface Temperature and Sea Ice Analysis (OSTIA) (Donlon et al. 2012).

Our free-running forecast experiments are initialized from the GEOS-5 FP assimilation state at 2100 UTC 12 September 2012, and are run for 10 days. Several hours prior to our forecast experiment initialization time, the HS3 "environmental" Global Hawk flew over Nadine for the first time during its transition from a tropical depression to a tropical storm from 11-12 September 2012. Figure 1 depicts the dust near developing Nadine, showing the daily composite 550-nm total aerosol optical thickness (AOT) on 12 September from MODIS Terra (Fig. 1a) and vertical profiles of 532-nm total attenuated backscatter from CPL onboard the Global Hawk (Fig. 1c). We note that neither the MODIS Terra nor Aqua sensors were able to observe dust on the western side of Nadine due to sun glint, or directly over Nadine due to the presence of clouds. Additionally, CPL was affected by glass moisture condensation on the instrument window and telescope, as well as attenuation by clouds during the first 4 legs of the flight over Nadine and the SAL, therefore only the components of the flight where dust was observed and CPL was not affected by lens condensation is shown. Despite these limitations, MODIS Terra observed a broad region of dust to the east of Nadine, which was also observed by CPL on the latter legs of the flight. Figure 1b shows the 550-nm total AOT from the GEOS-5 FP assimilation state nearest the MODIS Terra observation time at 1300 UTC 12 September, and Figure 1d shows the GEOS-5 simulated 532 nm total attenuated backscatter sampled along the Global Hawk track.

Where coincident with MODIS Terra, the GEOS-5 FP assimilation produces a similar spatial distribution and magnitude of AOT as shown in the MODIS data. Compared with CPL, GEOS-5 captures the magnitude and vertical extent of the elevated dust between 2-5 km, and when combined with the comparison to MODIS Terra, the GEOS-5 FP assimilation used to initialize the free running forecast simulations provides a realistic representation of the horizontal and vertical distribution of dust near Nadine.

The 10-day GEOS-5 simulation period covers the period of Nadine's strengthening from a tropical storm (30 m s^{-1}) to a hurricane (36 m s^{-1}) on 14 September, followed by the first weakening phase (15-22 September), notably weakening back to a tropical storm strength (30 m s^{-1}) on 17 September. The simulations are initialized on 12 September to allow aerosol feedback to Nadine to emerge during the first weakening phase, as Reale et al. (2014) found statistically significant aerosol impacts on storm vorticity after 5 days of simulation time.

5. Evaluation of Hurricane Nadine Simulations

Figure 2 shows the simulated track, minimum surface pressure, and maximum wind speed for the GEOS-5 forecasts and FP assimilation compared to the best track provided by the National Oceanic and Atmospheric Administration (NOAA) National Hurricane Center (NHC) (http://www.nhc.noaa.gov/data/tcr/AL142012_Nadine.pdf). Comparing GEOS-5 simulated tracks (Fig. 2a), we see that the FP assimilation matches the observed track very well, while there is variability between our forecasts both with respect to the observations and with each other. The NI and WA simulated tracks are comparable to one another and simulate Nadine farther to the east than observed. Additionally, this result shows that the less-absorbing dust has little impact on the simulated track compared to the NI simulation. However, comparing our

WA and SA simulations, we find a divergence in the simulated track beginning on 17 September, where the SA track turns to the north, showing that when only aerosol-radiation interaction is simulated, Nadine's track is indeed very sensitive to dust absorption, which is explored further in Section 6. The simulations that included two-moment microphysics (WACM, SACM) move more slowly to the east between 15-18 September compared to the NHC best track and the NI, WA, and SA simulations, but have better agreement with the NHC best track at the end of the 10 day simulation period. Most notably, unlike the simulations with only aerosol-radiation interaction, the WACM and SACM simulations showed little sensitivity to dust optical properties. Simulated GEOS-5 minimum surface pressure (Fig. 2b) and maximum wind speed (Fig. 2c) for the free-running forecast simulations are comparable to each other and the FP assimilation during the first 5 days of simulation, but then exhibit considerable variability coincident with divergence in their simulated tracks (Fig. 2a). Compared to observed intensity and minimum surface pressure, the simulated storms never reach Category 1 intensity and obtain their maximum wind speed and minimum surface pressure 3 days later than observed. Comparisons between simulated track, minimum surface pressure, and maximum wind speed show that our 25-km horizontal-resolution simulations reasonably represent the NHC best track track, but struggle to capture the timing of simulated minimum surface pressure and maximum wind speeds. We speculate that higher resolution simulations would improve the representation of storm dynamics, but we did not explore this here because of the computational expense.

On 14-15 September, the Global Hawk overflew Nadine (1500 UTC 14 September-1100 UTC 15 September) for a second time, immediately following Nadine's transition from a tropical storm (30 m s^{-1}) to a category 1 hurricane (36 m s^{-1}), despite strong environmental vertical wind shear and a notable SAL presence surrounding the system. Figure 3 shows the observed vertical profile of total attenuated backscatter from CPL along the flight track, and the co-located profiles from the GEOS-5 FP assimilation and free-running simulations. During the flight, segments of the CPL observations were again affected by lens condensation issues and attenuation by clouds, as indicated on the figure. Figure 4 shows the flight track overlaid on the corresponding simulated AOT. Due to similarity between the NI and WA simulations, we only show the WA simulation in both Figures 3 and 4. CPL observed elevated dust layers on several legs of the flight (Fig. 3), with the three regions of strongest backscatter near the eastern ends of the flight legs (Fig. 4). The variability of the CPL backscatter is captured in the GEOS-5 FP assimilation and the free running simulations. Additionally, the simulations exhibit little variability between one another during this time, as only 24-36 hours of simulation time has elapsed, but all indicate the presence of the elevated SAL near Nadine. We note that enhanced total attenuated backscatter near the surface in each GEOS-5 simulation is due to the presence of seasalt aerosol, resulting from strong surface winds over the ocean.

Figure 4 shows the dust AOT and surface pressure at 1700 UTC 14 September, and 850-hPa winds sampled at dropsonde locations and times along the Global Hawk track for the GEOS-5 simulations. In Fig. 4a, we show the observed AVAPS dropsonde winds at the 850-hPa pressure surface, with the GEOS-5 FP assimilation dust AOT and surface pressure overlaid (as in Fig. 4b), as MODIS observations of AOT surrounding Nadine were limited due to the presence of clouds on this day. Figure 4 shows the similarity between the GEOS-5 FP assimilation and all of the forecast simulations, showing the proximity of the dust-laden SAL near Hurricane Nadine, with dust wrapping from east to west along the northern side of the storm. While only 36 hours into the simulations, subtle differences between the experiments begin to emerge. First, there is more dust to the north and west of Nadine in the FP assimilation than in any of the forecasts.

This higher AOT is a direct result of assimilating AOT in prior days in the GEOS-5 FP assimilation, which corrects the simulated column mass loading when and where MODIS AOT observations are available. Next, there is less dust to the west of Nadine's center in the simulations that use the two-moment cloud microphysics (WACM and SACM) than in the simulations that do not (WA and SA). Finally, comparing the 850-hPa winds in Fig. 4, we find that while the wind fields between the forecasts are quite similar, subtle differences in wind speed and direction begin to emerge to the east and southeast of Nadine, where the dust AOT within the SAL is in close proximity to Nadine.

In Fig. 5, we show the wind profile for an AVAPS dropsonde (see triangle in Fig. 4) and the GEOS-5 simulated profiles within Nadine's tropical environment to the west of the boundary with the SAL, where we see subtle differences in simulated wind fields in close proximity to the SAL. While only a single dropsonde profile is shown, other nearby dropsonde profiles that sampled southerly flow associated with Nadine's tropical environment along the boundary with the SAL provided similar results. Comparing the GEOS-5 profiles to AVAPS, the two simulations that include the two-moment microphysics scheme (WACM, SACM) best match the observed wind speeds and directions, followed by the FP assimilation, which does not include two-moment microphysics but is impacted by the assimilation of meteorological observations. The simulations that do not include two-moment microphysics fail to capture the observed wind structure, and instead simulate a broad region of enhanced winds from near the surface to about 5 km.

6. Dust Impacts on the Track of Hurricane Nadine

While the Global Hawk flight on 14-15 September provide useful observations for validating our GEOS-5 forecasts, substantial differences between the simulated tracks are not evident until 17 September (Fig. 2), where the SA simulation diverts to the northwest compared to the other simulated tracks, demonstrating a sensitivity to the assumed dust optical properties in our simulations that only permit aerosol-radiation interaction. Here, we investigate the dynamical response responsible for the divergence in the SA track by performing a series of ensemble-like perturbations to the dust optical properties in the simulations that only permit aerosol-radiation interactions. We first replace the less absorbing dust with the more absorbing dust optical properties at 24-hour increments into the WA simulation. Similarly, we then replace the more absorbing dust with the less absorbing dust at 24-hour increments into the SA simulation. In Fig. 6, we show the sensitivity of Nadine's simulated track to these perturbations. All of the simulations starting with more absorbing dust (SA) move to the northwest late in the simulations no matter when the optical properties are switched to less absorbing dust. For the WA simulations, all move to the east no matter when the optical properties are switched to more absorbing dust. Thus, there is little impact on the simulated track, demonstrating that in both cases the perturbation to the dynamical environment occurs within the first 24 hours of the simulation, even though significant impacts on the track do not emerge until days 4-5.

We further targeted the source of the perturbation to Nadine's track in the SA experiment by performing additional ensemble-like perturbations, where the weakly absorbing dust was replaced with the strongly absorbing dust at 3 hour increments within the first 24 hours of simulation time. From these additional perturbations, we found that the simulation in which weakly absorbing dust was replaced with strongly absorbing dust at 0900 UTC 13 September yielded a track that followed the SA track, while a simulation making this switch at 1200 UTC

13 September yielded a track that followed WA (Fig. 7a). This result suggests that the difference in simulated tracks between the WA and SA simulations results from a shortwave radiative perturbation, as sunrise occurs between 0900 and 1200 UTC 13 September at the position of Nadine. Figure 7b shows the dust AOT from the simulation in which weakly absorbing dust was replaced by strongly absorbing dust at 1200 UTC 13 September (AOT is similar for all simulations at this time) and the 0-5 km vertically averaged 0900-1300 UTC total temperature difference [K] (shaded) due to aerosol shortwave radiative effects between WA simulations switched to more absorbing dust at 0900 and 1200 UTC at 1300 UTC 13 September 2012. We find an increase in temperature throughout the horizontal and vertical extent of the SAL due to shortwave absorption by dust where the highest dust AOT is in close proximity to Nadine in our simulation initialized at 0900 UTC, suggesting that the track deviation in the SA simulation results from a dynamical response related to the additional absorption by dust near sunrise.

We next explore the impact of the shortwave radiative temperature perturbation in the WA and SA simulations on the dynamical structure of Hurricane Nadine. Figure 8 shows Nadine's dynamic response to dust radiative forcing for both sets of dust optical properties by showing the storm centric meridional winds and shortwave radiative temperature tendency due to aerosols for west-east transects through the center of Nadine at times of notable storm structure difference during 13 – 17 September period for the WA and SA simulations. At 1800 UTC on 13 September, the vortex depth, meridional winds and dust concentrations are similar between the simulations, however, the SA aerosol shortwave temperature tendency within the dusty SAL is notably stronger when compared to the WA simulation. Two days later at 1800 UTC on 15 September, a secondary wind maximum above the aerosol shortwave temperature perturbation is evident in the SA simulation that is not yet present in the WA simulation. One day later at 1200

UTC 16 September, the secondary wind maximum emerges in the WA simulation, while there is a broad region of enhanced low-level southerly winds in the SA simulation. At this time, the WA and SA tracks begin to diverge (Fig. 2). Fig. 9, which shows the dust AOT, 850-hPa winds, and 850-hPa heights at 1200 UTC 16 September, and here we find greater westerly flow to the east of Nadine in close proximity to the SAL in the WA simulation, compared to the more southerly flow in the SA simulation. At 1200 UTC on 17 September, the storm structure in the WA simulation is similar to the SA structure on 16 September, while low-level southerly winds in the SA simulation extend to higher altitudes compared to the previous day. Owing to similar vortex depth between the WA and SA simulations between 13 – 17 September, storm centric meridional and zonal steering winds below 7 km within an 8° latitude by longitude box are shown in Fig. 10. Consistent with the timing of divergence between the WA and SA tracks, we find enhanced southerly steering flow beginning on 16 September in the SA simulation, one day prior to the WA simulation. The timing of the enhanced SA southerly steering flow coincides with the timing of the secondary wind maximum, suggesting that the storm is impacted by different steering currents owing to the size and structure of the storm. This result is consistent with previous studies by Fiorino and Elsberry (1989) and Chan and Gray (1982), who showed that the steering flow experienced by a tropical storm has a dependence on the size of the storm. Prior to 16 September, the zonal steering flow is comparable between the simulations, then diverge when the SA storm changes direction from an eastward to northwest trajectory.

Comparing the WA and SA simulations, simply varying dust absorption can impact storm size by introducing a larger shortwave temperature perturbation that induces a secondary wind maximum approximately 24 hours earlier than the simulation using the weakly absorbing dust, which has implications for the steering flow that the storm experiences. In this case, the impacts on the storm track are drastic, as the enhanced westerly and reduced southerly steering flow to the east of Nadine in the WA simulation on 16 September steers the system to interact with the trough to the east of Nadine in Fig. 9 on 17 September, leading to a rapid eastward track. In the case of the SA simulation, enhanced southerly steering flow on 16 September reduces Nadine's interaction with the trough on 17 September (Fig. 9), but rather steers the storm to the north, where the Azores High steers the storm to the northwest. Combining this with the sensitivity experiments presented in Fig. 7a, the shortwave temperature perturbation that impacts storm structure and steering flow that the storm experiences can be traced to the first few hours of sunlight on 13 September, with a dynamical response of the storm to the shortwave aerosol temperature perturbation delayed by approximately 2.5 days, followed by impacts on the storm track 2 days later.

In contrast to the simulations that only permitted aerosol-radiation interaction, the simulations that also included two-moment microphysics did not exhibit sensitivity to dust optical properties and best matched the observed track at the end of the 10 day simulation period. We now explore the mechanisms responsible for the differences between simulated tracks in the simulations with and without two-moment microphysics. To reiterate, the two-moment microphysics scheme predicts cloud and ice particle number concentration in response to simulated aerosol loading, in contrast to the single moment cloud microphysics scheme used in the WA and SA simulations that prescribes the particle size, number, and concentration of the condensate (Barahona et al. 2014). For dust, which was treated as an INP in the forecasts, the effect of implementing the two-moment microphysics is shown in Fig. 11, where the MODIS Terra ice cloud effective radius at 1330 UTC on 13 September 2012 is compared to simulated retrievals of MODIS cloud products for the SA and SACM simulations using the Cloud

Feedback Model Intercomparison Project Observation Simulator Package (COSP, Bodas-Salcedo et al. 2011). Comparing the simulated retrievals of MODIS ice cloud effective radius between the SA and SACM simulations (Fig. 11), the spatial distribution of simulated ice cloud effective radii better represents the observations (Fig. 11a) in the SACM simulation (Fig. 11c) than in the SA simulation (Fig. 11b). Modifications to ice cloud effective radius are known to impact the radiative budget of the atmosphere (Quaas et al. 2008; Rotstayn 1999; Jones and Slingo 1996), and in Fig. 12, the shortwave aerosol, longwave cloud, and net (shortwave + longwave) total atmospheric radiative forcings are shown for the SA and SACM simulation at 1300 UTC on 13 September 2012. The shortwave forcing is nearly identical in both simulations, but there is enhanced longwave cooling in the SACM simulation owing to the two-moment microphysics scheme. In the SA simulation, the relatively lower longwave cooling from clouds means the net atmospheric radiative forcing has a larger contribution from the shortwave forcing, while in the SACM simulation the net effect near Nadine is dominated by longwave cooling which overcomes the shortwave warming that introduces the temperature perturbation and subsequent dynamical response impacting the storm track in the SA simulation.

The effects of including the two-moment microphysics scheme is also evident in the vertical structure of Nadine beginning on 14 September (not shown), as a deeper vortex with thicker ice and water clouds at higher altitudes is simulated in the two-moment microphysics simulations. This has implications for the steering winds in the WACM and SACM simulations, as we see reduced zonal steering flow (Fig. 10) in the simulations that include two-moment microphysics from 14 September to 17 September. The reduced zonal steering flow allows Nadine to remain over warmer SSTs (Fig 2a.) for a longer period of time, leading to further vertical development and a more intense storm in the WACM and SACM simulations (Fig. 2b & Fig. 2c).

Additionally, the reduced zonal steering flow in the WACM and SACM simulations delays the interaction between Nadine and the trough to the east of the system (Fig. 9), slowing its eastward translational speed, allowing for the Azores High to steer Nadine to the south at the end of each simulation (Fig. 2a).

Finally, as added perturbation experiments, we performed two additional SACM simulations, one where the number concentration of dust INP was reduced to 10% and another where dust was permitted to act as a CCN in addition to INP with a CCN efficiency similar to the more hygroscopic dust from Asian deserts (κ=0.2, Kumar et al., 2009). Figure 13 shows the simulated tracks for the perturbations compared to the observed, SA, and baseline SACM tracks, and we find that while enabling dust as a CCN has little impact on simulated track, while reducing the number of available dust INP to 10% yields a track that diverts to the northwest, though later than the SA simulation. Combined with Figs. 11 and 12, this result shows that the lack of track sensitivity to dust optical properties in the WACM and SACM simulations results from indirect effects of dust acting as an efficient INP, yielding a more realistic representation of clouds.

7. Conclusions

In this study, we used the NASA GEOS-5 atmospheric general circulation model and assimilation system to simulate the impacts of dust on the first intensification (12– 15 September) and weakening phases (15 – 22 September) of Hurricane Nadine (2012) during HS3. Compared to MODIS and CPL observations from the first HS3 flight on 11-12 September, the GEOS-5 FP assimilation accurately characterized the horizontal and vertical distribution of dust near Nadine. Several forecast experiments were initialized from the GEOS-5 FP assimilation where the nature of the aerosol-atmosphere interaction was varied (no interactive, aerosol-radiation interaction, aerosol-radiation and aerosol-cloud interaction via two-moment microphysics), as well as the absorption of our assumed dust optical properties.

We found that when only aerosol-radiation interactions were permitted, Nadine's track exhibited sensitivity to dust optical properties. Through a series of ensemble-like perturbations where our weakly absorbing dust optical properties were replaced with strongly absorbing dust optical properties (and vice versa) we found that this sensitivity was established in the first hours following the initialization of the simulation, coincident with the first sunrise after simulation initialization (Figs. 6 and 7). Further analysis showed that dust optical properties with stronger absorption in the shortwave induced a temperature perturbation that impacted the timing of Nadine's structure and size, which had implications for the steering winds that Nadine experienced (Figs. 8, 9, and 10), and consequently, the interaction of Nadine with large-scale synoptic features, ultimately affecting the track. Our findings demonstrated that the shortwave aerosol temperature perturbation incurred during the first sunrise after initialization resulted in a dynamical response in Nadine's structure approximately 2.5 days later, followed by subsequent impacts on Nadine's trajectory 5 days after initialization. These findings support Reale et al., (2014), who demonstrated that impacts on tropical cyclogenesis from aerosol-radiation interaction were significant after 5 days of simulation time.

Our best match with the observed wind structure was obtained by implementing two-moment microphysics in conjunction with aerosol-radiation interaction. In these simulations, we found very little sensitivity to assumed dust optical properties and comparing the shortwave aerosol atmospheric forcing to the longwave cloud atmospheric forcing showed enhanced longwave cooling from clouds that negates shortwave aerosol atmospheric forcing surrounding Nadine resulting from to the implementation of the two-moment microphysics scheme, suggesting that radiative effects resulting from aerosol-radiation interaction are secondary to aerosol-cloud interaction for this case study. Finally, as added perturbations, the impacts of permitting dust to act as a CCN and reducing the number of dust INP by 10% in simulations using two-moment microphysics with a more absorbing dust were explored. We found that permitting dust to act as a CCN had little impact on Nadine's track, while reducing the number of dust INP by 10% yielded a diverted track similar to our aerosol-radiation simulation (SA) using the more absorbing dust. This finding demonstrated that the lack of sensitivity of Nadine's track to dust optical properties using the two-moment microphysics scheme results from a more realistic representation of clouds when dust acts as an effective INP. In contrast, the simulations that use the single moment scheme simulate less realistic clouds and consequently, owing to a reduced cloud radiative forcing, exhibit a greater sensitivity to aerosol radiative effects compared to the real atmosphere. This finding highlights the importance of including dust interactions as an INP in simulations of tropical systems developing near the SAL.

We acknowledge that our findings are the result of one series of forecast simulations for a specific case and that more robust results would be found considering additional case studies where dust was in close proximity to developing tropical systems. However, for this specific case, our series of ensemble-like perturbations where dust optical properties were modified at different times during the simulation helps to give significance to our finding that absorption by dust can impact storm tracks when only aerosol-radiation interaction is permitted in global aerosol simulations. Finally, our findings highlight the importance of including dust-atmosphere interactions, particularly dust-radiation and aerosol-cloud interactions, when simulating tropical systems in proximity to the SAL. This may be a particular consideration for operational forecasting centers that do not include aerosol interaction in their forecasts, as our simulations demonstrate that the degree of dust interaction can have significant impacts on the track of tropical systems.

Acknowledgements. We would like to thank Oreste Reale for valuable discussion on simulating tropical systems with aerosol interactions using GEOS-5. This work and the HS3 mission was funded by NASA's Earth Venture Suborbital program at NASA Headquarters. Simulations were performed at the NASA Center for Climate Simulation (NCCS).

8. References

Balkanski, Y., M. Schulz, T. Claquin, and S. Guibert, 2007: Reevaluation of Mineral aerosol radiative forcings suggests a better agreement with satellite and AERONET data, *Atmospheric Chemistry and Physics*, *7*(1), 81-95.

Barahona, D., J. Rodriguez, and A. Nenes, 2010a: Sensitivity of the global distribution of cirrus ice crystal concentration to heterogeneous freezing, J. Geophys. Res., 115, D23213, doi:10.1029/2010JD014273.

Barahona, D., Molod, A., Bacmeister, J., Nenes, A., Gettelman, A., Morrison, H., Phillips, V., and Eichmann, A., 2014: Development of two-moment cloud microphysics for liquid and ice within the NASA Goddard Earth Observing System Model (GEOS-5), *Geosci. Model Dev.*, 7, 1733-1766, doi:10.5194/gmd-7-1733-2014.

Bodas-Salcedo, A., and Coauthors, 2011: COSP: Satellite simulation software for model assessment. *Bulletin of the American Meteorological Society*, *92*(8), 1023-1043.

Braun, S. A., Newman, P. A., and Heymsfield, G. M., 2016: NASA's Hurricane and Severe Storm Sentinel (HS3) Investigation. *Bulletin of the American Meteorological Society*, (2016).

Braun, S. A., Sippel, J. A., Shie, C. L., and Boller, R. A., 2013: The evolution and role of the Saharan Air Layer during Hurricane Helene (2006). *Monthly Weather Review*, *141*(12), 4269-4295.

Bretl, S., Reutter, P., Raible, C. C., Ferrachat, S., Poberaj, C. S., Revell, L. E., and Lohmann, U., 2015: The influence of absorbed solar radiation by Saharan dust on hurricane genesis. *Journal of Geophysical Research: Atmospheres*, *120*(5), 1902-1917.

Buchard, V., da Silva, A. M., Colarco, P., Krotkov, N., Dickerson, R. R., Stehr, J. W., Mount, G., Spinei, E., Arkinson, H. L. and He, H, 2014: Evaluation of GEOS-5 sulfur dioxide simulations during the Frostburg, MD 2010 field campaign, *Atmos Chem Phys*, 14(4), 1929–1941, doi:10.5194/acp-14-1929-2014.

Buchard, V., da Silva, A., Colarco, P., Darmenov, A., Govindaraju, R., Torres, O., Campbell, J., and Spurr, R., 2015: Using OMI Aerosol Index and Aerosol Absorption Optical Depth to Evaluate the NASA MERRA Aerosol Reanalysis, *Atmos. Chem. Phys*., 15, 5743-5760, doi: 10.5194/acp-15-5743-2015.

Burpee, R. W., 1972: The origin and structure of easterly waves in the lower troposphere of North Africa. *Journal of the Atmospheric Sciences*, *29*(1), 77-90.

Carlson, T. N., and Prospero, J. M., 1972: The large-scale movement of Saharan air outbreaks over the northern equatorial Atlantic. *Journal of applied meteorology*, *11*(2), 283-297.

Chan, J. C., and Gray, W. M., 1982: Tropical cyclone movement and surrounding flow relationships. *Monthly Weather Review*, *110*(10), 1354-1374.

Chen, T. C., Wang, S. Y., and Clark, A. J., 2008: North Atlantic hurricanes contributed by African easterly waves north and south of the African easterly jet. *Journal of Climate*, *21*(24), 6767-6776.

Chin, M., and Coauthors, 2002: Tropospheric aerosol optical thickness from the GOCART model and comparisons with satellite and Sun photometer measurements. Journal of the atmospheric sciences, 59(3), 461-483.

Chou, M.-I. and M. Suarez, 1994: An efficient thermal infrared radiation parameterization for use in general circulation models. *NASA Tech. Mem. 104606,* 3, Technical Report Series on Global Modcling and Data Assimilation. 85 pp.

Colarco, P., da Silva, A., Chin, M., and Diehl, T., 2010: Online simulations of global aerosol distributions in the NASA GEOS-4 model and comparisons to satellite and ground-based aerosol optical depth, *J. Geophys. Res*., 115, D14207, doi:10.1029/2009JD012820.

Colarco, P. R., Nowottnick, E. P., Randles C. A., Yi, B., Yang, P., Kim, K.-M., Smith, J. A., and Bardeen, C. G., 2014: Impact of radiatively interactive dust aerosols in the NASA GEOS-5 climate model: Sensitivity to dust particle shape and refractive index, *J. Geophys. Res. Atmos*., 119, 753–786, doi:10.1002/2013JD020046.

DeMott, P. J., Sassen, K., Poellot, M. R., Baumgardner, D., Rogers, D. C., Brooks, S. D., Prenni, A. J., and Kreidenweis, S. M., 2003: African dust aerosols as atmospheric ice nuclei, *Geophys. Res. Lett.*, 30, 1732, doi:10.1029/2003GL017410, 14.

Donlon, C. J., Martin, M., Stark, J., Roberts-Jones, J., Fiedler, E., and Wimmer, W., 2012: The operational sea surface temperature and sea ice analysis (OSTIA) system, *Remote Sens. Environ.*, 116, 140–158, doi:10.1016/j.rse.2010.10.017.

Dunion, J. P., and Velden, C. S., 2004: The impact of the Saharan air layer on Atlantic tropical cyclone activity. *Bulletin of the American Meteorological Society*, *85*(3), 353-365.

Evan, A. T., Dunion, J., Foley, J. A., Heidinger, A. K., and Velden, C. S., 2006: New evidence for a relationship between Atlantic tropical cyclone activity and African dust outbreaks. *Geophysical Research Letters*, *33*(19).

Evan, A. T., and Coauthors, 2008: Ocean temperature forcing by aerosols across the Atlantic tropical cyclone development region. *Geochemistry, Geophysics, Geosystems*, *9*(5).

Fiorino, M., and Elsberry, R. L., 1989: Some aspects of vortex structure related to tropical cyclone motion. *Journal of the atmospheric sciences*, *46*(7), 975-990.

Hess, M., Koepke, P., and Schult, I., 1998: Optical properties of aerosols and clouds: The software package OPAC. *Bulletin of the American meteorological society*, *79*(5), 831-844.

Hill, C., DeLuca, C., Balaji, V., Suarez, M., da Silva, A., and the ESMF Joint Specification Team, 2004: The Architecture of the Earth System Modeling Framework, *Computing in Sci. and Eng.*, 6, 1-6.

Hock, T. F., and Franklin, J. L., 1999: The ncar gps dropwindsonde. *Bulletin of the American Meteorological Society*, *80*(3), 407-420.

Jenkins, G. S., and Pratt, A., 2008: Saharan dust, lightning and tropical cyclones in the eastern tropical Atlantic during NAMMA-06. *Geophysical Research Letters*, *35*(12).

Jenkins, G. S., Pratt, A. S., and Heymsfield, A., 2008: Possible linkages between Saharan dust and tropical cyclone rain band invigoration in the eastern Atlantic during NAMMA-06. *Geophysical Research Letters*, *35*(8).

Jones, A., and Slingo, A., 1996: Predicting cloud-droplet effective radius and indirect sulphate aerosol forcing using a general circulation model. *Quarterly Journal of the Royal Meteorological Society*, *122*(535), 1573-1595.

Jones, C., Mahowald, N., and Luo, C., 2003: The role of easterly waves on African desert dust transport. *Journal of Climate*, *16*(22), 3617-3628.

Karyampudi, V. M., and Coauthors, 1999: Validation of the Saharan dust plume conceptual model using lidar, Meteosat, and ECMWF data. *Bulletin of the American Meteorological Society*, *80*(6), 1045-1075.

Kiladis, G. N., Thorncroft, C. D., and Hall, N. M., 2006: Three-dimensional structure and dynamics of African easterly waves. Part I: Observations. *Journal of the Atmospheric Sciences*, *63*(9), 2212-2230.

Knippertz, P., and Todd, M. C., 2010: The central west Saharan dust hot spot and its relation to African easterly waves and extratropical disturbances. *Journal of Geophysical Research: Atmospheres*, *115*(D12).

Kumar, P., Nenes, A., and Sokolik, I. N., 2009: Importance of adsorption for CCN activity and hygroscopic properties of mineral dust aerosol. *Geophysical Research Letters*, *36*(24).

Lance, S., Nenes, A., and Rissman, T. A., 2004: Chemical and dynamical effects on cloud droplet number: Implications for estimates of the aerosol indirect effect, *J. Geophys. Res*., 109, D22208, doi:10.1029/2004JD004596.

Lau, K. M., and Kim, K. -M., 2007: Cooling of the Atlantic by Saharan dust. *Geophysical Research Letters*, *34*(23).

Levy, R. C., Remer, L. A., Kleidman, R. G., Mattoo, S., Ichoku, C., Kahn, R., and Eck, T. F., 2010: Global evaluation of the Collection 5 MODIS dark-target aerosol products over land, *Atmos. Chem. Phys.*, 10, 10,399–10,420, doi:10.5194/acp-10-10399-2010.

McGill, M. J., Hlavka, D. L., Hart, W. D., Scott, V. S., Spinhirne, J., and Schmid, B., 2002: Cloud physics lidar: Instrument description and initial measurement results, *App. Opt.*, 41, 3725–3734.

Meng, Z., Yang, P., Kattawar, G. W., Bi, L., Liou, K. N., and Laszlo, I., 2010: Single-scattering properties of tri-axial ellipsoidal mineral dust aerosols, A database for application to radiative transfer calculations, *Journal of Aerosol Science*, 41(5), 501-512.

Morrison, H., and Gettelman, A., 2008: A new two-moment bulk stratiform cloud microphysics scheme in the Community Atmosphere Model, version 3 (CAM3). Part I: Description and numerical tests. *Journal of Climate*, *21*(15), 3642-3659.

Munsell, E. B., Sippel, J. A., Braun, S. A., Weng, Y., and Zhang, F., 2015: Dynamics and predictability of Hurricane Nadine (2012) evaluated through convection-permitting ensemble analysis and forecasts. *Monthly Weather Review*, *143*(11), 4514-4532.

Nowottnick, E., Colarco, P., Ferrare, R., Chen, G., Ismail, S., Anderson, B., and Browell, E., 2010: Online simulations of mineral dust aerosol distributions: Comparisons to NAMMA observations and sensitivity to dust emission parameterization. *Journal of Geophysical Research: Atmospheres*, *115*(D3).

Nowottnick, E., Colarco, P., da Silva, A., Hlavka, D., and McGill, M., 2011: The Fate of Saharan Dust Across the Atlantic and Implications for a Central American Dust Barrier, *Atmos. Chem. Phys.*, *11*, 8415-8431, doi:10.5194/acp-11-8415-2011.

Nowottnick, E. P., Colarco, P .R., Welton, E. J., and da Silva, A., 2015: Use of the CALIOP vertical feature mask for evaluating global aerosol models, *Atmos. Meas. Tech*., 8, 3647–3669, doi:10.5194/amt-8-3647-2015.

Quaas, J., Boucher, O., Bellouin, N., and Kinne, S., 2008: Satellite-based estimate of the direct and indirect aerosol climate forcing. *Journal of Geophysical Research: Atmospheres*, *113*(D5).

Randles, C. A., da Silva, A., Buchard, V., Colarco, P. R., Darmenov, A. S., Govindaraju, R. C., Smirnov, A., Ferrare, R. A., Hair, J. W., Shinozuka, Y., and Flynn, C., 2016: The MERRA-2 Aerosol Reanalysis, 1980-onward, Part I: System Description and Data Assimilation Evaluation. J. Clim.

Reale, O., Lau, K. M., Kim, K. -M., and Brin, E., 2009: Atlantic tropical cyclogenetic processes during SOP-3 NAMMA in the GEOS-5 global data assimilation and forecast system, *J. Atmos. Sci.*, 66, 3563–3578, doi:10.1175/2009JAS3123.1.

Reale, O., Lau, K. M., and da Silva, A., 2011: Impact of an interactive aerosol on the African easterly jet in the NASA GEOS-5 global forecasting system, *Weather Forecast.*, 26(4), 504–519, doi:10.1175/WAF-D-10-05025.1.

Reale, O., Lau, K. M., da Silva, A., and Matsui, T., 2014: Impact of assimilated and interactive aerosol on tropical cyclogenesis, *Geophys. Res. Lett.*, 41, 3282–3288, doi:10.1002/2014GL059918.

Remer, L. A., and Coauthors, 2005: The MODIS aerosol algorithm, products, and validation, *J. Atmos. Sci.*, 62, 947–973, doi:10.1175/JAS3385.1.

Rienecker, M. M., and Coauthors, 2008: The GEOS-5 Data Assimilation System—Documentation of versions 5.0.1 and 5.1.0, and 5.2.0. NASA Tech. Rep. Series on Global Modeling and Data Assimilation, NASA/TM-2008-104606, Vol. 27, 92 pp.

Rosenfeld, D., Rudich, Y., and Lahav, R., 2001: Desert dust suppressing precipitation: A possible desertification feedback loop. *Proceedings of the National Academy of Sciences*, *98*(11), 5975-5980.

Rotstayn, L. D., 1999: Indirect forcing by anthropogenic aerosols: A global climate model calculation of the effective-radius and cloud-lifetime effects. *Journal of Geophysical Research: Atmospheres*, *104*(D8), 9369-9380.

Thorncroft, C., and Hodges, K., 2001: African easterly wave variability and its relationship to Atlantic tropical cyclone activity. *Journal of Climate*, *14*(6), 1166-1179.

Twohy, C. H., 2015: Measurements of Saharan dust in convective clouds over the tropical eastern Atlantic Ocean. *Journal of the Atmospheric Sciences*, *72*(1), 75-81.

Wong, S., Dessler, A. E., Mahowald, N. M., Yang, P., and Feng, Q., 2009: Maintenance of lower tropospheric temperature inversion in the Saharan air layer by dust and dry anomaly. *Journal of Climate*, *22*(19), 5149-5162.

Zhang, H., McFarquhar, G. M., Saleeby, S. M., and Cotton, W. R., 2007: Impacts of Saharan dust as CCN on the evolution of an idealized tropical cyclone. *Geophysical Research Letters*, *34*(14).

9. Tables

Table 1

Experiment Name	Experiment Description	Dust Optical Properties
NI	Non-Interactive Aerosols	N/A
WA	Aerosol Direct Interaction w/Less Absorbing Dust	Observation Based [Colarco et al., 2014]
WACM	Aerosol Direct Interaction w/Less Absorbing Dust and 2-Moment Microphysics	Observation Based [Colarco et al., 2014]
SA	Aerosol Direct Interaction w/More Absorbing Dust	OPAC [Hess et al., 1998]
SACM	Aerosol Direct Interaction w/More Absorbing Dust and 2-Moment Microphysics	OPAC [Hess et al., 1998]

Table 1. Experiment name, description, and dust optical properties for GEOS-5 aerosol perturbation forecasts of Hurricane Nadine.

10. Figure Caption List

Figure 1. MODIS Terra 550 nm AOT on 12 September 2012 (a), GEOS-5 FP assimilation total AOT at 1400 UTC on 12 September (b), CPL 532 nm total attenuated backscatter from the 11-12 September HS3 flight (c), and GEOS-5 FP assimilation 532 nm total attenuated backscatter sampled coincident 11-12 September HS3 flight (d). The portion of the Global Hawk flight track depicted in the CPL and GEOS-5 cross sections is indicated by the red lines in (a) and (b). The red "x" indicates the position of Nadine at 1200 UTC on 12 September 2012 from the National Hurricane Center (a) and in the GEOS-5 FP assimilation (b).

Figure 2. NHC Best Track and GEOS-5 simulated tracks over simulation averaged OSTIA SSTs [K] (a), minimum surface pressure (b), and storm intensity (c) for Hurricane Nadine (12-22 September 2012).

Figure 3. CPL (a), GEOS-5 FP assimilation (b), WA (c), SA (d), WACM (e), and SACM (f) simulated profiles of total attenuated backscatter from the 14-15 September 2012 HS3 flight. Global Hawk track and GEOS-5 FP assimilation dust AOT is inset in (b). Components of CPL observations affected by lens condensation and signal attenuation by clouds is indicated by "C" and "A", respectively. Portions of the flight where CPL observed elevated dust layers are indicated by the red line.

Figure 4. AVAPS 850-hPa winds over GEOS-5 FP assimilation dust AOT and surface pressure contoured at 1010 and 1000 hPa (a); 850-hPa winds, dust AOT, and minimum pressure for the

GEOS-5 FP assimilation (b), WA (c), SA (d), WACM (e), and SACM (f) simulations for the 14-15 September HS3 flight. The location of the individual dropsonde profile in Fig. 5 is indicated by the black triangle. Half-barb, full-barb, and flags indicate wind speeds of 2.5 m s^{-1}, 5 m s^{-1}, and 25 m s^{-1}, respectively.

Figure 5. Wind profiles from AVAPS (a), the GEOS-5 FP assimilation (b), NI (c), WA (d), SA (e), WACM (f), and SACM (g) simulations at the drop location indicated on Figure 3 during the 14-15 September 2012 HS3 flight. Half-barb, full-barb, and flags indicate wind speeds of 2.5 m s^{-1}, 5 m s^{-1}, and 25 m s^{-1}, respectively.

Figure 6. WA and SA sensitivity experiment track where dust optical properties were changed at 24-hour increments in each simulation overlaid on mean (12-22 September) OSTIA SSTs [K].

Figure 7. (a) WA experiment track where weakly absorbing dust optical properties were replaced with strongly absorbing dust optical at 0900 (dash) and 1200 UTC (solid) on 13 September 2012 over mean (12-22 September 2012) OSTIA SSTs [K]. (b) Dust AOT (contour) at 1200 UTC and the 0-5 km vertically averaged 0900-1300 UTC total temperature difference [K] (shaded) due to aerosol shortwave radiative effects between WA simulations switched to more absorbing dust at 0900 and 1200 UTC at 1300 UTC 13 September 2012.

Figure 8. WA (left) and SA (right) west-east storm-centric transects of meridional winds (shaded) and shortwave temperature tendency perturbation due to aerosols (dashed-dot contour 0.25 K dy^{-1}; solid 0.5 K dy^{-1}; dashed 1 K dy^{-1}).

Figure 9. WA (left), SA (center), and SACM (right) dust aerosol optical thickness (shaded contours), 850-hPa winds (arrows), and 850-hPa height (meters, black contour) at 1200 UTC on 16 September 2012.

Figure 10. WA, SA, WACM, and SACM meridional (a) and zonal (b) steering winds.

Figure 11. MODIS Terra (a), COSP simulated SA (b), and COSP simulated SACM (c) ice cloud effective radius at 1330 UTC on 13 September 2012. 1010 hPa contours (black) from the GEOS-5 FP assimilation, SA, and SACM simulations to indicate the position of Nadine are provided in (a), (b), and (c), respectively.

Figure 12. SA (top) and SACM (bottom) shortwave aerosol atmospheric forcing (left), longwave cloud atmospheric forcing (center), and net total atmospheric forcing (right) at 1300 UTC on 13 September 2012. 1010 hPa contours (black) indicate the position of Nadine in the SA and SACM simulations at 1300 UTC on 13 September 2012.

Figure 13. Simulated tracks for SACM with dust as a CCN (yellow) and SACM with the concentration of dust INP reduced by 90% (orange) relative to NHC Best Track (black), SA (blue), and SACM (purple) tracks over mean (12-22 September 2012) OSTIA SSTs [K].

11. Figures

Figure 1.

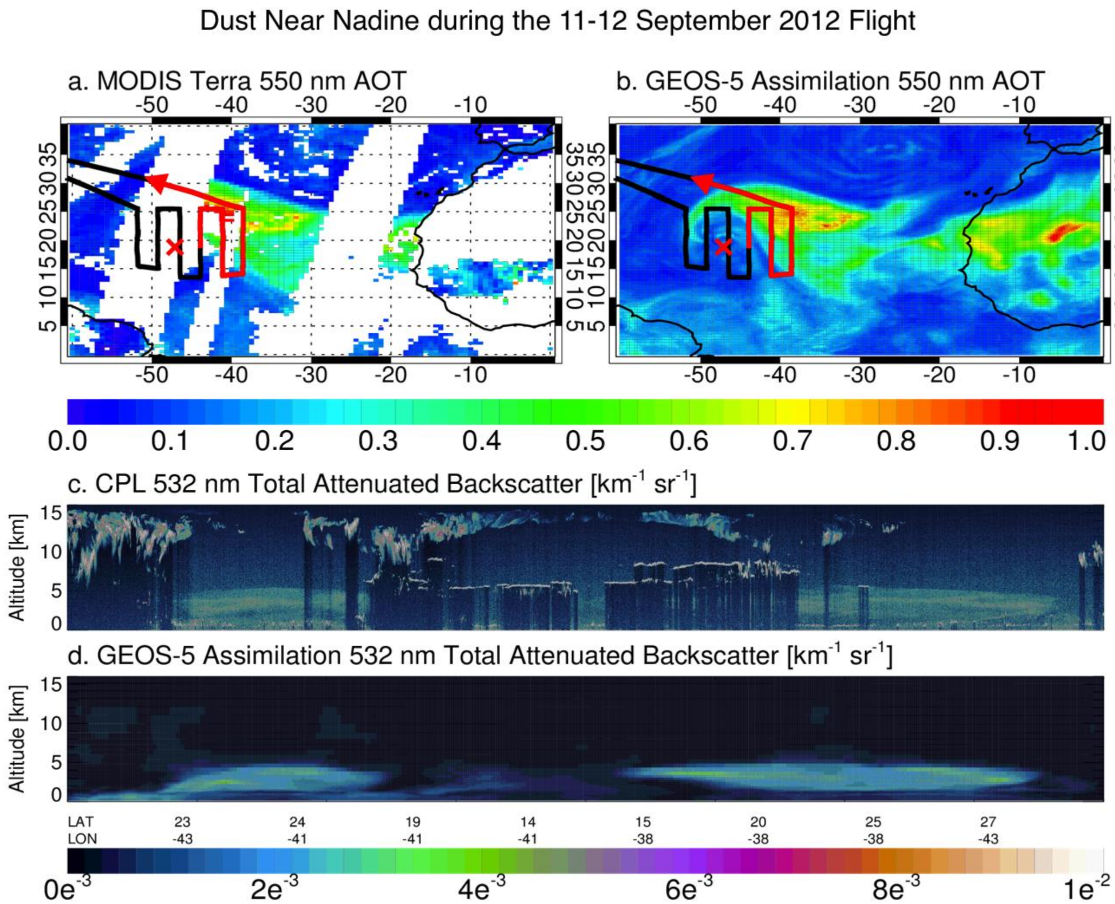

Figure 1. MODIS Terra 550 nm AOT on 12 September 2012 (a), GEOS-5 FP assimilation total AOT at 1400 UTC on 12 September (b), CPL 532 nm total attenuated backscatter from the 11-12 September HS3 flight (c), and GEOS-5 FP assimilation 532 nm total attenuated backscatter sampled coincident 11-12 September HS3 flight (d). The portion of the Global Hawk flight track depicted in the CPL and GEOS-5 cross sections is indicated by the red lines in (a) and (b). The red “x” indicates the position of Nadine at 1200 UTC on 12 September 2012 from the National Hurricane Center (a) and in the GEOS-5 FP assimilation (b).

Figure 2.

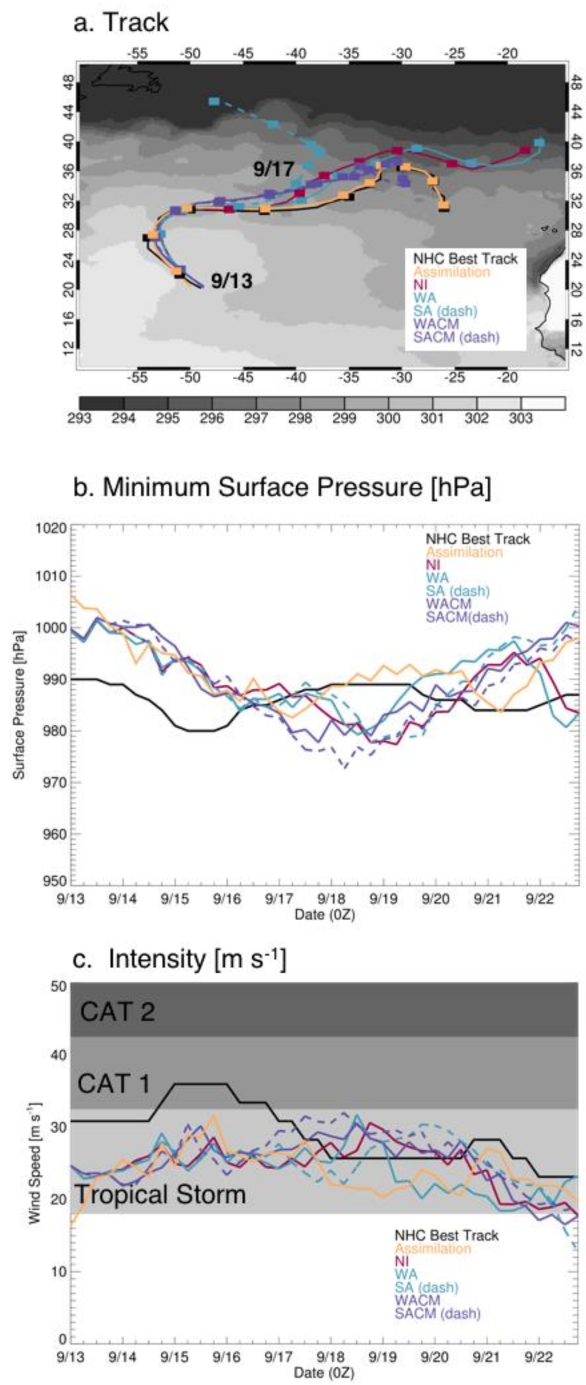

Figure 2. NHC Best Track and GEOS-5 simulated tracks over simulation averaged OSTIA SSTs [K] (a), minimum surface pressure (b), and storm intensity (c) for Hurricane Nadine (12-22 September 2012).

Figure 3.

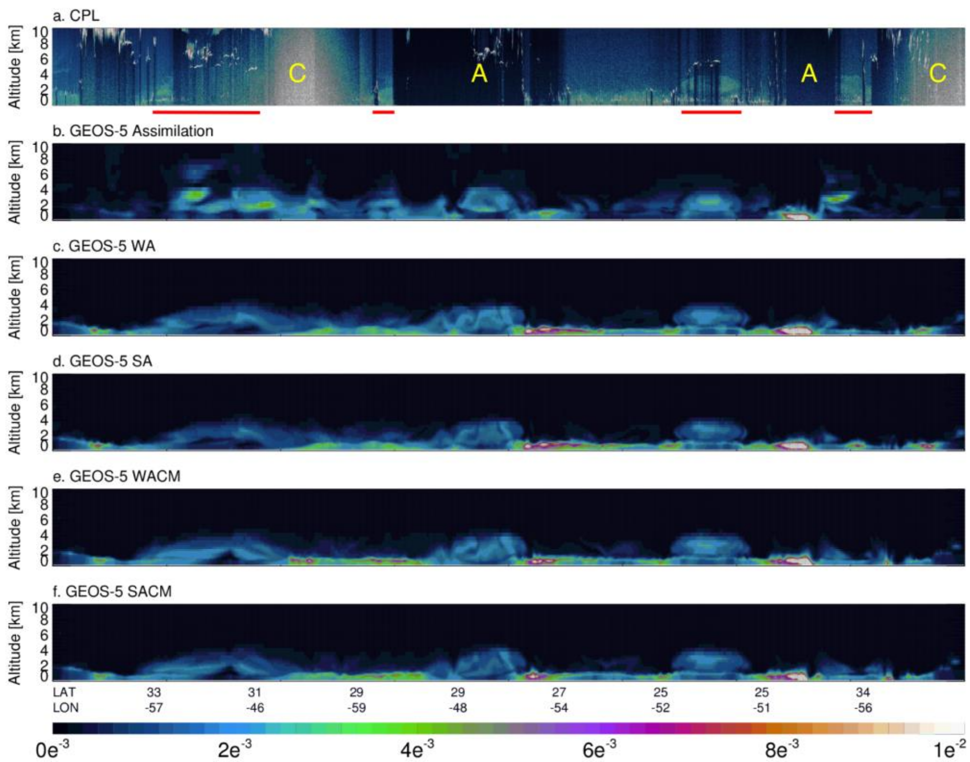

Figure 3. CPL (a), GEOS-5 FP assimilation (b), WA (c), SA (d), WACM (e), and SACM (f) simulated profiles of total attenuated backscatter from the 14-15 September 2012 HS3 flight. Global Hawk track and GEOS-5 FP assimilation dust AOT is inset in (b). Components of CPL observations affected by lens condensation and signal attenuation by clouds is indicated by “C” and “A”, respectively. Portions of the flight where CPL observed elevated dust layers are indicated by the red line.

Figure 4.

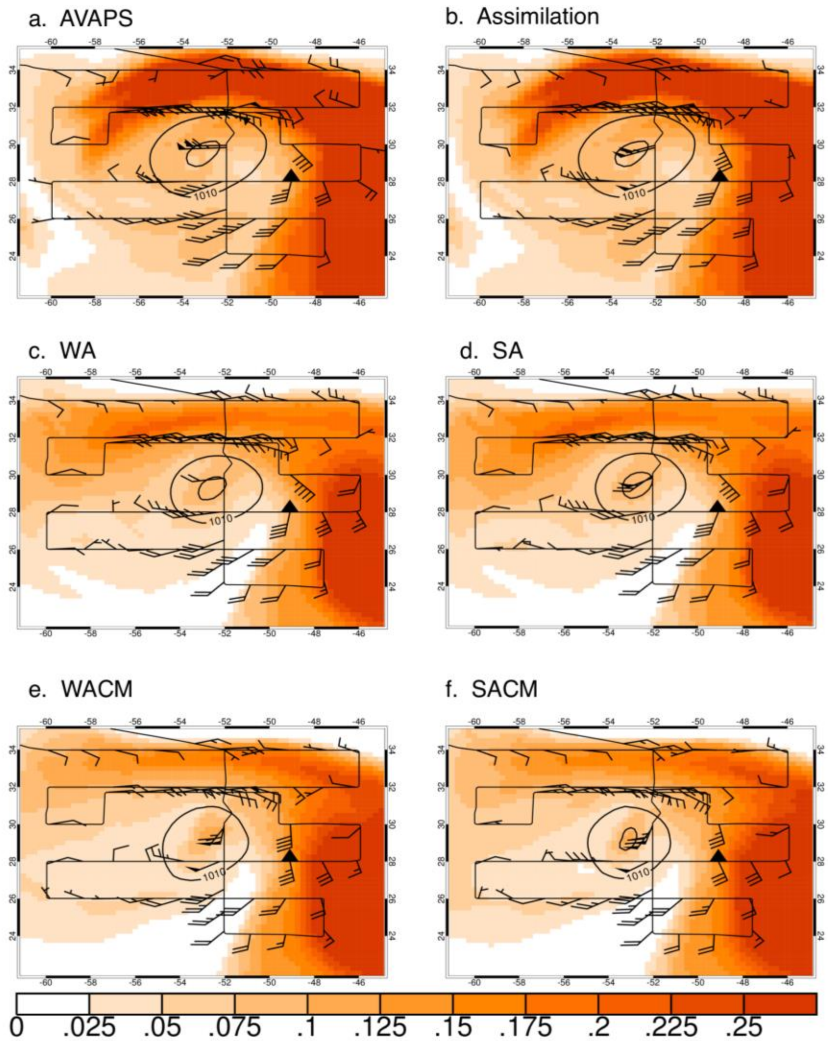

Figure 4. AVAPS 850-hPa winds over GEOS-5 FP assimilation dust AOT and surface pressure contoured at 1010 and 1000 hPa (a); 850-hPa winds, dust AOT, and minimum pressure for the GEOS-5 FP assimilation (b), WA (c), SA (d), WACM (e), and SACM (f) simulations for the 14-15 September HS3 flight. The location of the individual dropsonde profile in Fig. 5 is indicated by the black triangle. Half-barb, full-barb, and flags indicate wind speeds of 2.5 m s^{-1}, 5 m s^{-1}, and 25 m s^{-1}, respectively.

Figure 5.

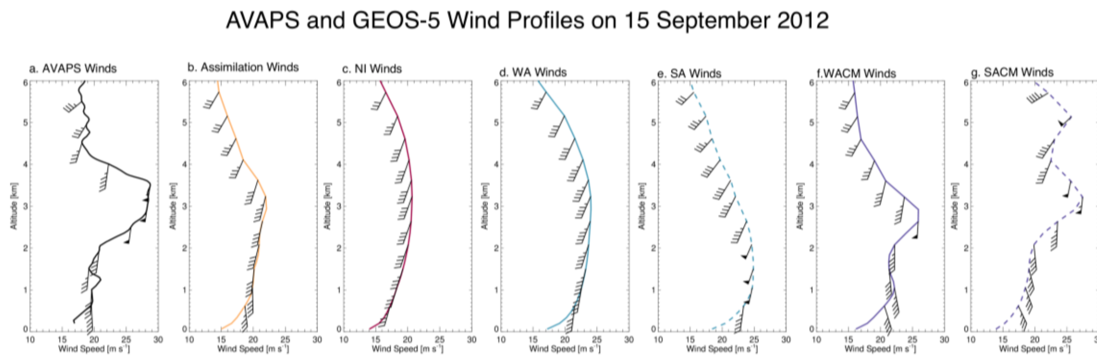

Figure 5. Wind profiles from AVAPS (a), the GEOS-5 FP assimilation (b), NI (c), WA (d), SA (e), WACM (f), and SACM (g) simulations at the drop location indicated on Figure 3 during the 14-15 September 2012 HS3 flight. Half-barb, full-barb, and flags indicate wind speeds of 2.5 m s^{-1}, 5 m s^{-1}, and 25 m s^{-1}, respectively.

Figure 6.

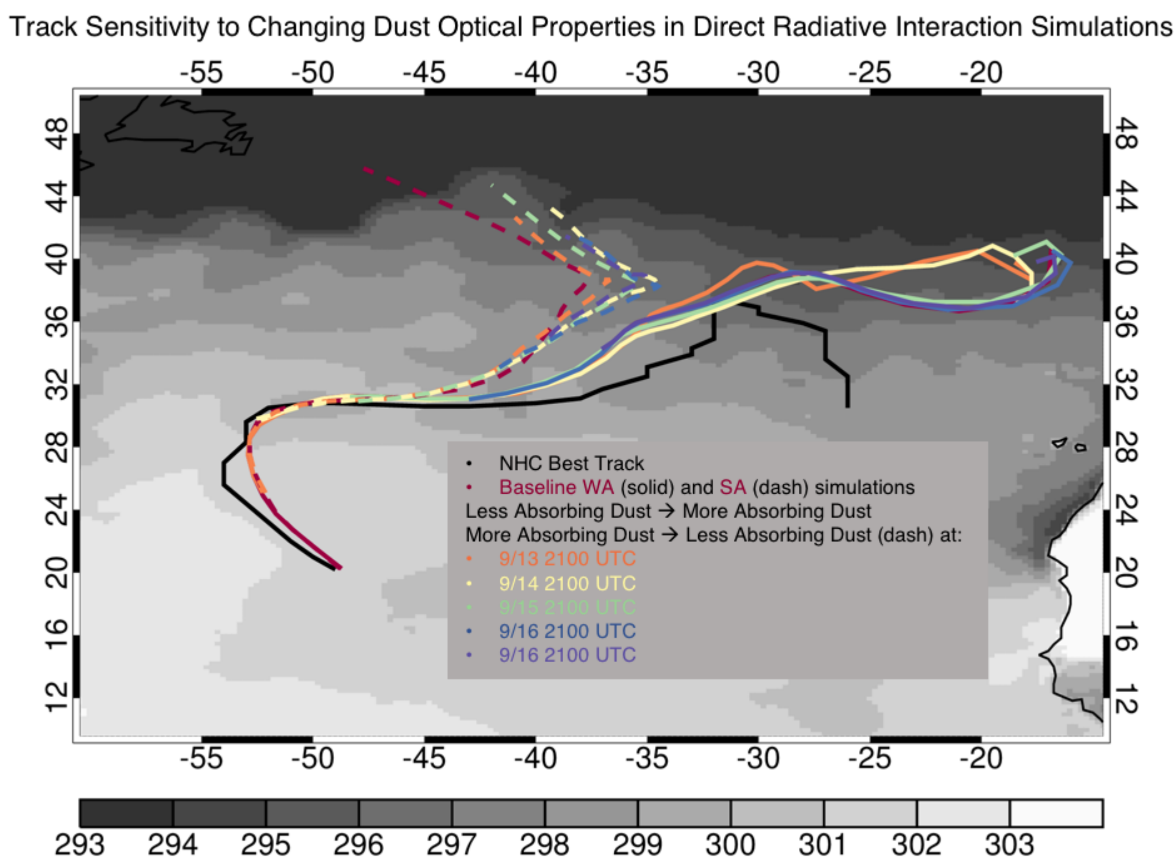

Figure 6. WA and SA sensitivity experiment track where dust optical properties were changed at 24-hour increments in each simulation overlaid on mean (12-22 September) OSTIA SSTs [K].

Figure 7.

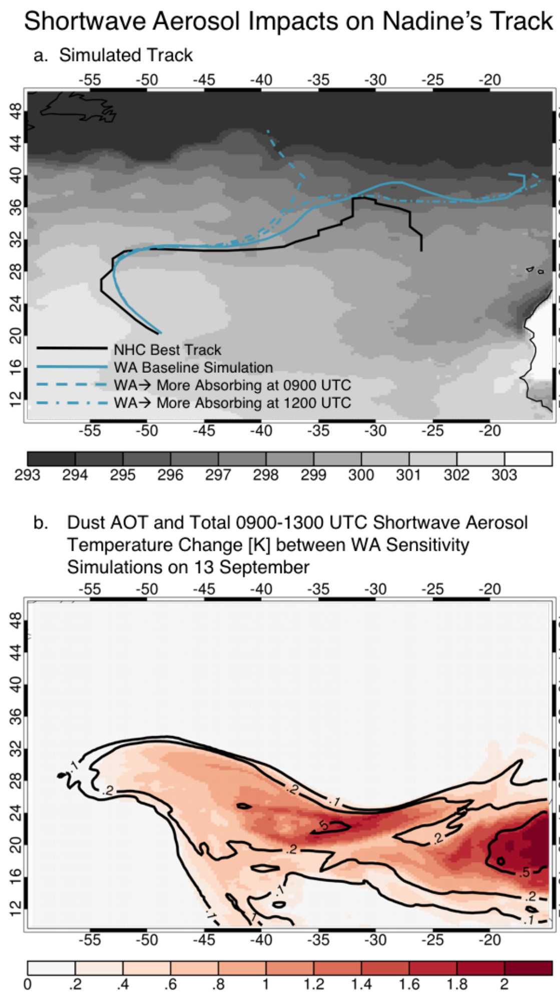

Figure 7. (a) WA experiment track where weakly absorbing dust optical properties were replaced with strongly absorbing dust optical at 0900 (dash) and 1200 UTC (solid) on 13 September 2012 over mean (12-22 September 2012) OSTIA SSTs [K]. (b) Dust AOT (contour) at 1200 UTC and the 0-5 km vertically averaged 0900-1300 UTC total temperature difference [K] (shaded) due to aerosol shortwave radiative effects between WA simulations switched to more absorbing dust at 0900 and 1200 UTC at 1300 UTC 13 September 2012.

Figure 8.

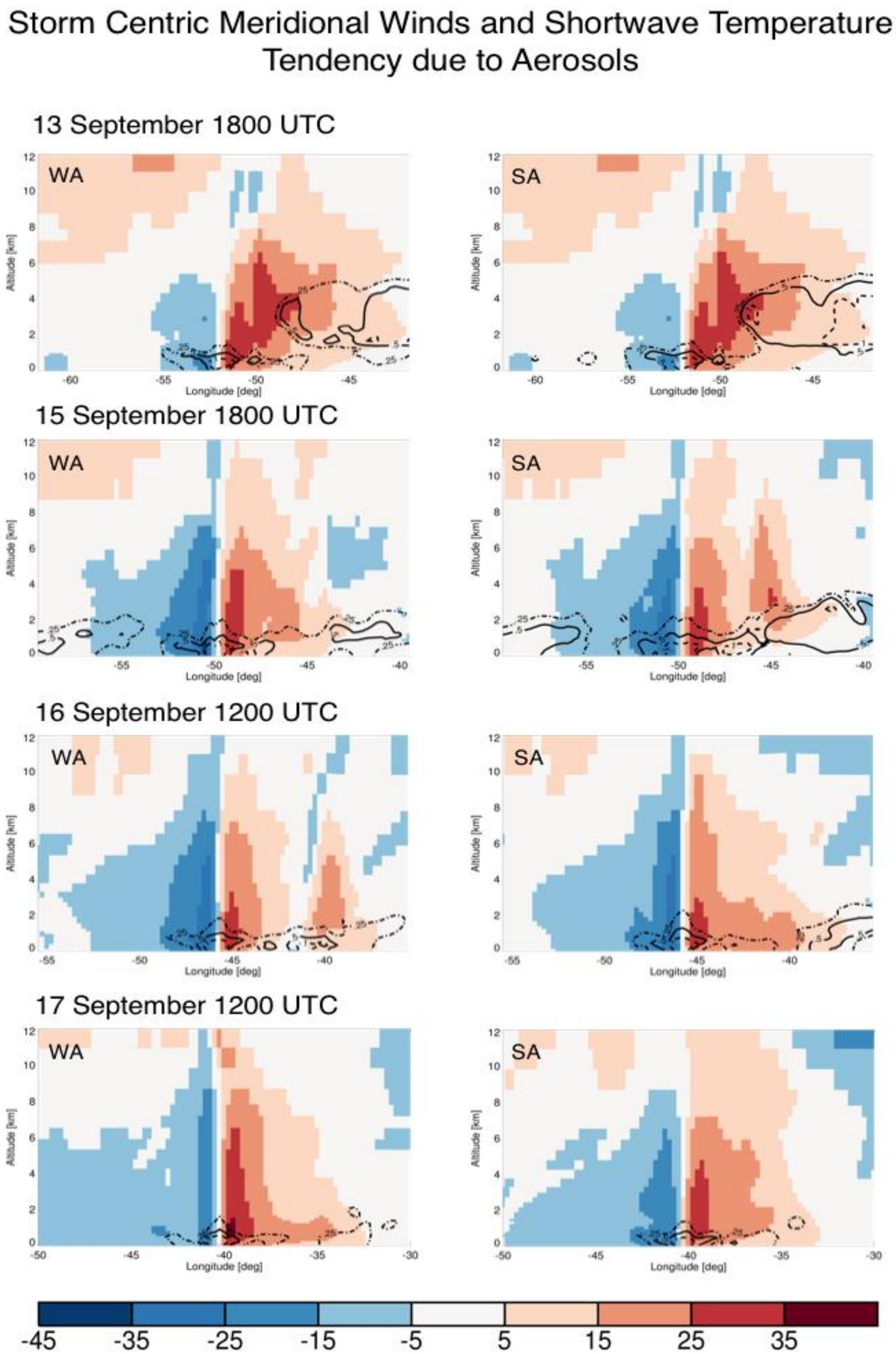

Figure 8. WA (left) and SA (right) west-east storm-centric transects of meridional winds (shaded) and shortwave temperature tendency perturbation due to aerosols (dashed-dot contour 0.25 K dy^{-1}; solid 0.5 K dy^{-1}; dashed 1 K dy^{-1}).

Figure 9.

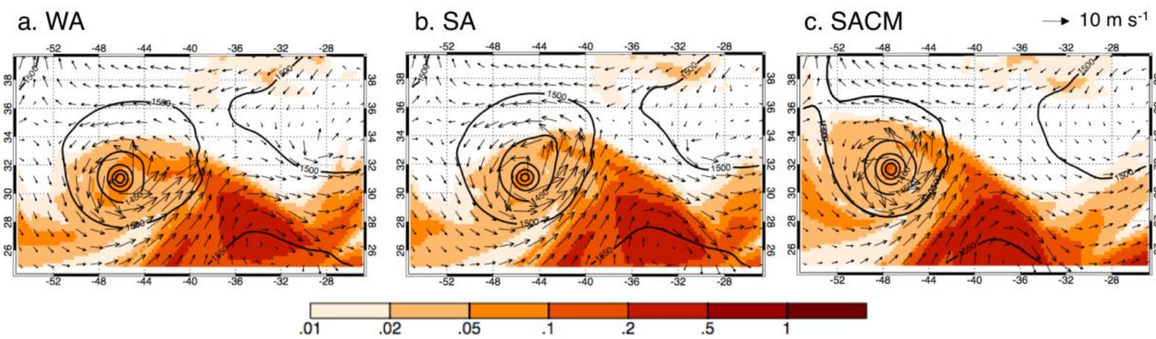

Figure 9. WA (left), SA (center), and SACM (right) dust aerosol optical thickness (shaded contours), 850-hPa winds (arrows), and 850-hPa height (meters, black contour) at 1200 UTC on 16 September 2012.

Figure 10.

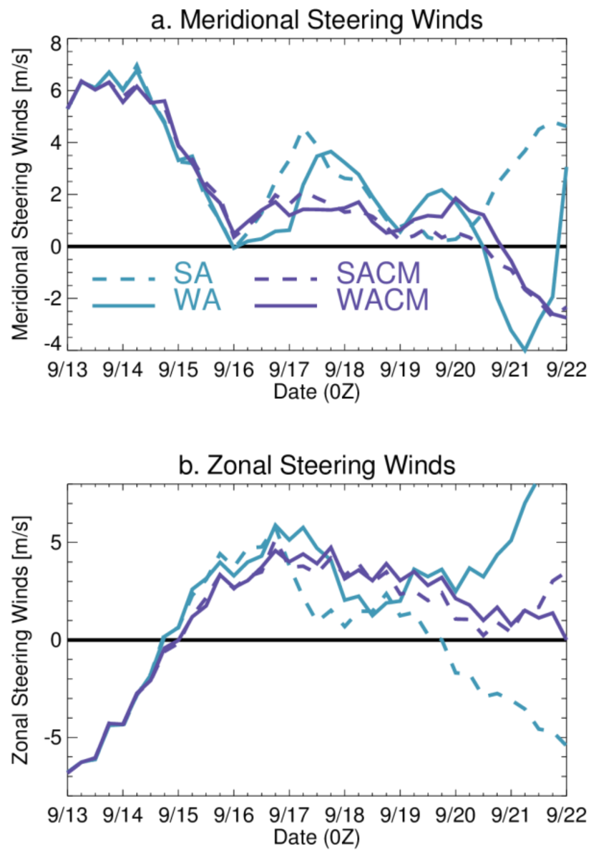

Figure 10. WA, SA, WACM, and SACM meridional (a) and zonal (b) steering winds.

Figure 11.

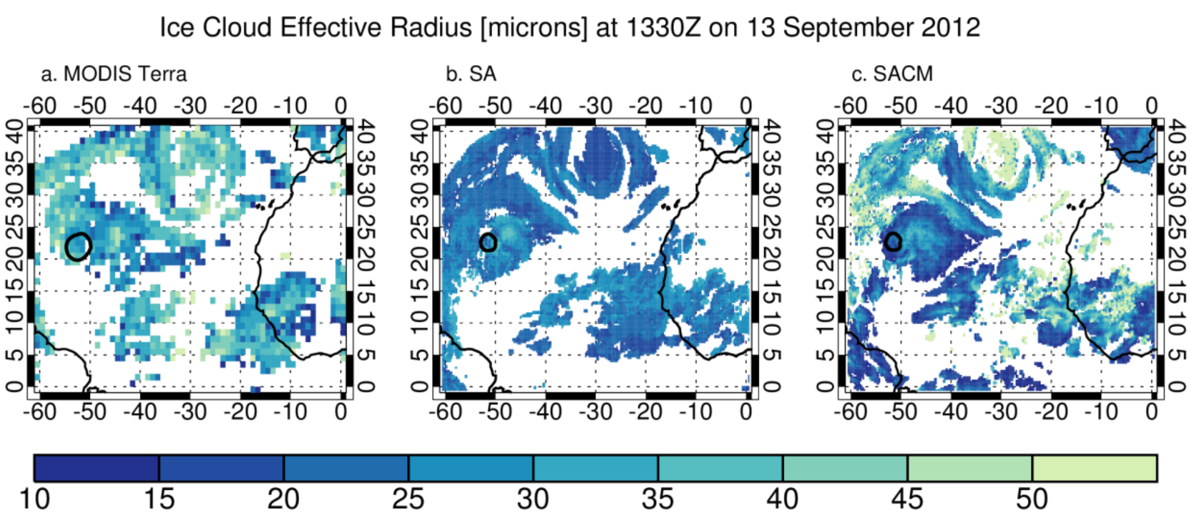

Figure 11. MODIS Terra (a), COSP simulated SA (b), and COSP simulated SACM (c) ice cloud effective radius at 1330 UTC on 13 September 2012. 1010 hPa contours (black) from the GEOS-5 FP assimilation, SA, and SACM simulations to indicate the position of Nadine are provided in (a), (b), and (c), respectively.

Figure 12.

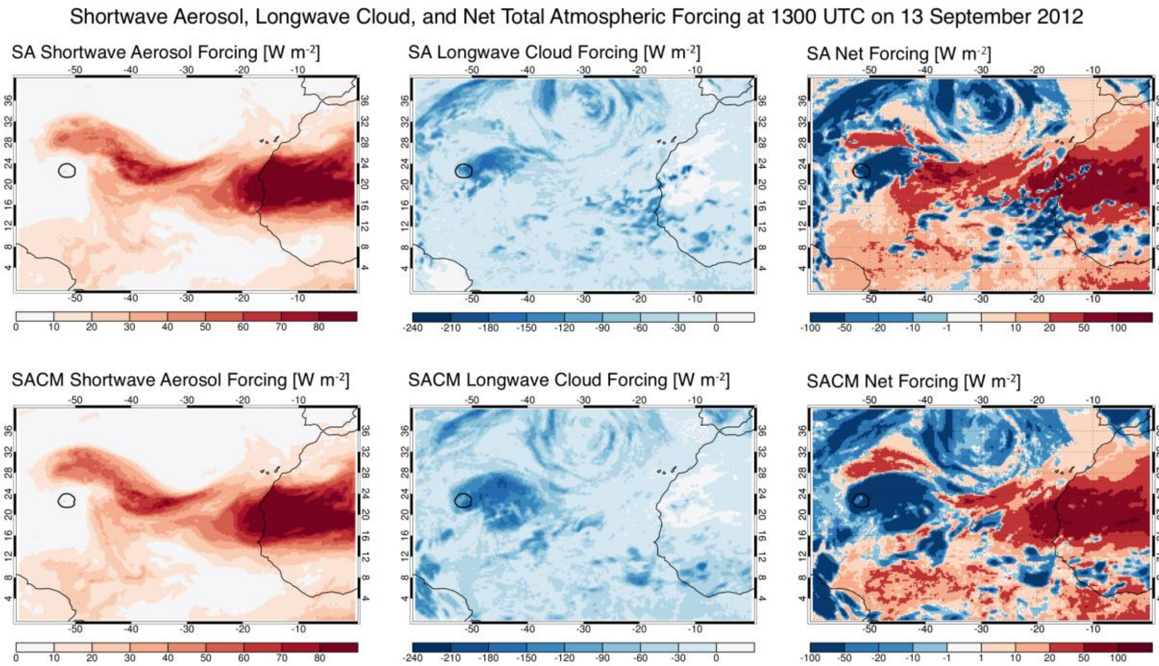

Figure 12. SA (top) and SACM (bottom) shortwave aerosol atmospheric forcing (left), longwave cloud atmospheric forcing (center), and net total atmospheric forcing (right) at 1300 UTC on 13 September 2012. 1010 hPa contours (black) indicate the position of Nadine in the SA and SACM simulations at 1300 UTC on 13 September 2012.

Figure 13.

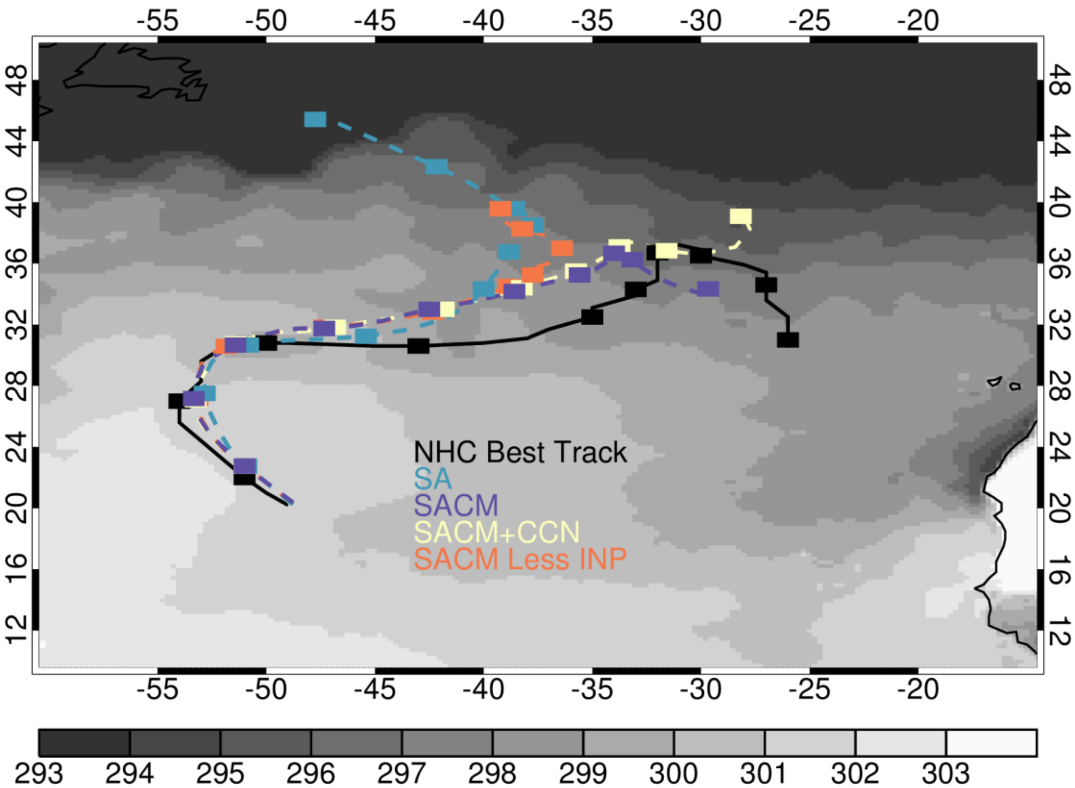

Figure 13. Simulated tracks for SACM with dust as a CCN (yellow) and SACM with the concentration of dust INP reduced by 90% (orange) relative to NHC Best Track (black), SA (blue), and SACM (purple) tracks over mean (12-22 September 2012) OSTIA SSTs [K].